Heating Rates in Tropical Anvils

THOMAS P. ACKERMAN

Space Science Division, NASA Ames Research Center, Moffett Field, California

KUO-NAN LIOU

Department of Meteorology, University of Utah, Salt Lake City

FRANCISCO P. J. VALERO AND LEONHARD PFISTER

Space Science Division, NASA Ames Research Center, Moffett Field, California

(Manuscript received 1 December 1986, in final form 28 December 1987)

ABSTRACT

The interaction of infrared and solar radiation with tropical cirrus anvils is addressed. Optical properties of the anvils are inferred from satellite observations and from high-altitude aircraft measurements. An infrared multiple-scattering model is used to compute heating rates in tropical anvils. Layer-average heating rates in 2 km thick anvils were found to be on the order of 20 to 30°K day^{-1}. The difference between heating rates at cloud bottom and cloud top ranges from 30 to 200°K day^{-1}, leading to convective instability in the anvil. The calculations are most sensitive to the assumed ice water content, but also are affected by the vertical distribution of ice water content and by the anvil thickness. Solar heating in anvils is shown to be less important than infrared heating but not negligible. The dynamical implications of the computed heating rates are also explored and we conclude that the heating may have important consequences for upward mass transport in the tropics. The potential impact of tropical cirrus on the tropical energy balance and cloud forcing are discussed.

1. Introduction

The influence of cirrus clouds on radiation exchange in the atmosphere is generally recognized as being important; however, due to various observational constraints (e.g., their height in the atmosphere), relatively few experimental studies of cirrus clouds have been carried out, particularly in the tropics. While it is apparent from satellite imagery that large portions of the tropics are covered by extensive cirrus systems (for example, see Liou 1986), the systems vary spatially and temporally. For example, cirrus formations associated with mesoscale complexes may have large vertical extents with bases near 5 to 6 km and tops between 12 and 16 km. These formations evolve during the life cycle of the complex. At various stages, they may consist of a midlevel deck with an overlying thinner anvil near the tropopause, a single deep deck (which may have substantial variations in ice crystal density with altitude), or a single elevated deck in the upper troposphere. This type of tropical anvil system has been observed in Venezuela (Betts 1973) and during Winter MONEX (Webster and Stephens 1980; Houze et al. 1981; Johnson and Kriete 1982). Alternatively, the cirrus may be anvils produced by the outflow of one or, possibly, a few deep convective cells. These anvils may have large gradations in thickness ranging from several kilometers in the vicinity of turrets to a kilometer or less near the edge of the formation (Danielsen 1982a; Margozzi 1983).

Satellite imagery clearly shows that large anvil complexes modify the planetary radiation budget by increasing the planetary albedo and reducing the infrared emission. Unfortunately, it is difficult to accurately quantify planetary effects from satellite imagery alone, and very little can be ascertained about the radiative exchange within the anvil. Griffith et al. (1980) and Webster and Stephens (1980) have indicated that cirrus decks can produce large local variations in atmospheric heating rates with heating at cloud bottom and cooling at cloud top. However, both these studies were confined to cirrus clouds below about 12 km, rather than the high cirrus near the tropical tropopause. More recently, Platt et al. (1984, 1987) have presented the results of several weeks of observations of tropical cirrus during March at Darwin, including a number of case studies. They used a ground-based lidar and an infrared narrow-beam radiometer to measure the vertical extent and infrared emissivity of cirrus clouds, including some with tops extending to 16 km. Aircraft observations in

Corresponding author address: Thomas Ackerman, The Pennsylvania State University, 503 Walker Building, Dept. of Meteorology, University Park, PA 16802.

© 1988 American Meteorological Society

Panama with the NASA U-2 (Margozzi 1983) and Darwin with the NASA ER-2 (unpublished data, Stratosphere Troposphere Exchange Project (STEP), January, 1987) show cloud tops extending to 17 and 18 km on several occasions. As will be discussed in the following section, these altitudes are consistent with satellite observations of brightness temperature. For a given optical thickness per kilometer, high cirrus produce greater extremes in the heating rate than do cirrus below 12 km due to the lower air density. Cirrus complexes are also likely to affect radiative heating in the stratosphere by reducing the outgoing infrared flux but increasing the reflected solar flux. Given the large horizontal extent of tropical cirrus, it is not implausible that these changes in radiative heating can have a substantial effect on atmospheric processes. For instance, Danielsen (1982b) has suggested that dehydration of stratospheric air occurs, in part, through radiative destabilization of high altitude anvils.

In order to quantify the radiative effect of tropical cirrus and assess its likely impact on the tropical atmosphere, we have carried out a theoretical study of radiative transfer in cirrus clouds. While we have attempted to incorporate the available measurements, their scarcity has made it difficult to define precisely the value of many of the variables, particularly ice water content (IWC). This in turn affects our estimates of typical cirrus optical depths. In order to establish some plausible limits on values of cirrus optical depth and IWC, we first present a simple computation of cirrus cloud optical depths based on infrared satellite imagery. We then perform a sensitivity analysis of the most important parameters to determine the effect of variations in their values on radiative transfer and heating rates.

2. Inferences from infrared satellite imagery

The infrared (wavelength interval of 10.5 to 12.6 μm) satellite image shown in Fig. 1a was taken at 1333 UTC 12 September 1980. The area covered extends roughly from 3° to 14°N and from 72° to 85°W. The coastal outlines of Central and South America are shown for reference. The grey tones or shadings in the image indicate the infrared brightness temperatures. (Brightness temperature is defined as the temperature of a blackbody that would emit the observed radiance in the given spectral interval.) The brightness temperatures range from a minimum of less than −77° to 20° → 30°C. The minimum temperatures are associated with the anvil complex located in the Gulf of Panama in the bottom center of the image. The maximum temperatures occur over the tropical ocean in the upper right.

The anvil complex in the Gulf is very large. The diameter of the northerly anvil is about 2° of latitude (or longitude) or about 220 km; the more southerly anvil is even larger. For easier interpretation, the grey tones in the more northerly anvil have been converted to shadings (Fig. 1b). The coldest temperature occurs in the center of the anvil and, as can be determined from visible imagery (not shown here), is associated with a turret, presumably produced by deep convection. Successively warmer brightness temperatures are found in approximately concentric rings around the cold core. Also shown in Fig. 1b is the flight track with beginning and ending times of a NASA U-2 airplane that flew above and into the anvil. The data acquired by the aircraft will be discussed in a subsequent section.

Because the minimum brightness temperature in the image is so cold (less than 196 K) and because only that portion of the atmosphere which is near the tropical tropopause reaches such low temperatures, the observed radiation must originate very near the tropopause (within a kilometer or so). Furthermore, it follows that the cloud from which this radiation originates has an emissivity approaching one within this same region of the atmosphere. If this were not the case, the brightness temperature would have to be greater than 196 K because radiation from the relatively warmer regions of the troposphere below the cloud would be transmitted through the cloud. An emissivity of near one within a kilometer or so of the tropopause implies an optical depth of at least two within this same geometric depth. In this particular case, we have radiosonde profiles and aircraft observations which confirm that the observed tropopause temperature was about 195 K or −78°C at an altitude of 17 km and that the cloud top was indeed located at the tropopause (see Fig. 3 and associated discussion in the following sections).

Of somewhat more interest within the context of this study is the gradual increase in brightness temperature as one moves from the cold central core towards the edges of the anvil system. One would logically assume that the cloud top height is roughly constant over this entire area since the anvil is formed by outflow from convective cells penetrating to the tropopause region. This is in fact confirmed both by the visible satellite imagery and by pilot reports from the NASA U-2 aircraft (Margozzi 1983; see also the following section). Given this approximately constant cloud top height, the observed increasing brightness temperatures imply a decreasing optical depth. (It is possible that the increasing brightness temperature could result from some combination of a constant cirrus optical depth and a variable midtroposphere cloud deck. However, this seems rather unlikely given the type of deep convective cells observed in the area and the lack of a plausible scenario for generating the required highly organized midlevel deck.)

If we assume that there are no mid- or low-level clouds between the surface and the overlying cirrus (with the exception of the deep convective cells), we can use the fact that the atmosphere is essentially transparent in the wavelength region of the satellite observation to express the observed radiance as

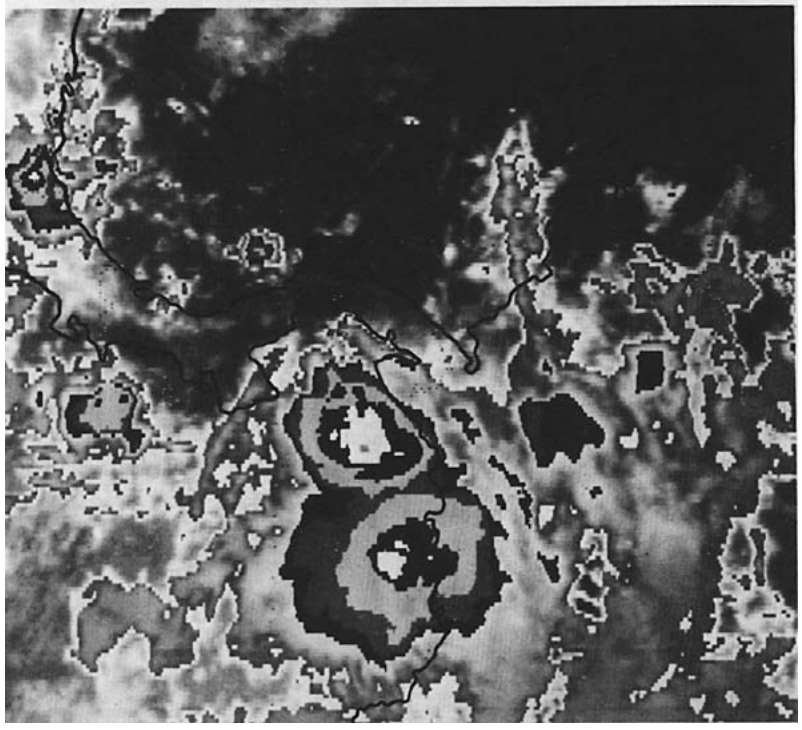

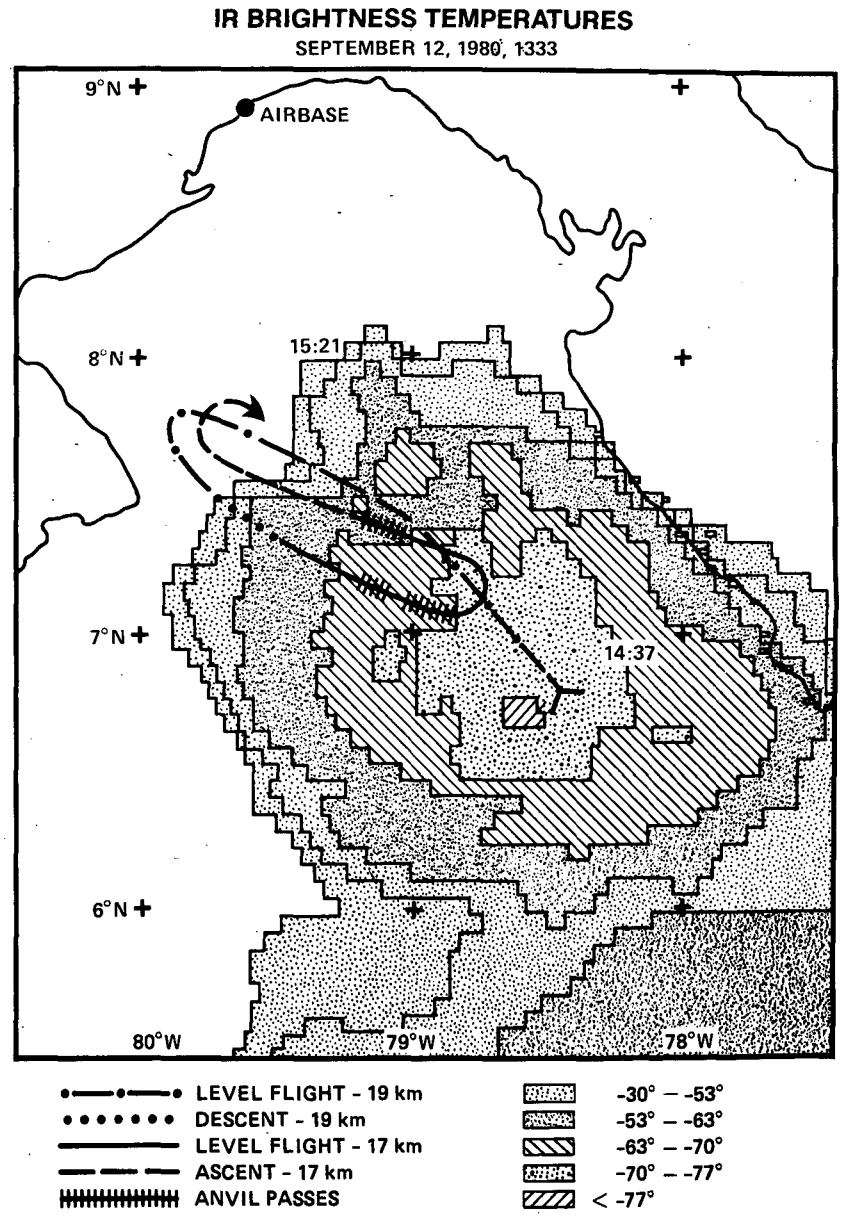

FIG. 1. (a) A portion of an infrared (wavelength interval of 10.5 to 12.6 μm) satellite image from GOES taken at 1333 UTC 12 September 1980, covering roughly the area from 3° to 14°N latitude and from 72° to 85°W longitude. The coastal outlines of Central and South America are shown for reference. A large anvil complex is shown located in the Gulf of Panama in the bottom center of the image. Brightness temperatures are indicated by grey tones ranging from a minimum of less than −77°C (the small grey area in the center of the more northerly anvil) to 20° → 30°C (the dark grey to black area at the top center and right of the image). (b) An enlargement of the northerly anvil in the Gulf of Panama. For clarity, brightness temperatures are depicted by shadings indicated in the legend. The flight path of the NASA U-2 is shown by a heavy line and annotated in the figure legend.

$$B_e(\mu) = B_s e^{-\tau/\mu} + \int_0^\tau e^{-\tau'/\mu} S(\tau') \frac{d\tau'}{\mu} \quad (1)$$

where B_e is the observed radiance, B_s is the radiance emitted from the surface (assumed to be isotropic), τ is the cloud optical depth, and μ is the cosine of the viewing angle. The source function $S(\tau')$ is at a depth τ' in the cloud. If we now approximate $S(\tau')$ by a two-stream source function (Toon et al. 1977, 1988) and assume that the cirrus cloud is isothermal, Eq. (1) becomes

$$B_e(\mu) = B_s e^{-\tau/\mu} + B_c(1 - e^{-\tau/\mu}) + B_s\delta_s(\mu, \tau) - B_c\delta_c(\mu, \tau) \quad (2)$$

where B_c is the radiance of a blackbody at the cirrus cloud temperature. Clearly, the first two terms on the right represent the transmission and thermal emission of a nonscattering medium. The third term represents an increase in the transmission of the incident radiation into the viewing direction due to scattering, while the last term combines a reduction from blackbody emission due to scattering and the effects of internal scattering. The coefficients of these latter two terms are written as

$$\delta_s = \frac{f^- - \Gamma^2 f^+}{2D} \quad (3)$$

$$\delta_c = (1 - \Gamma e^{-\lambda\tau}) \frac{f^- + e^{\lambda\tau}\Gamma f^+}{2D} \quad (4)$$

where

$$\lambda = 2(1 - \gamma)^{1/2}$$

$$\gamma = \varpi(1 - g)$$

$$\Gamma = \frac{(2 - \lambda)}{(2 + \lambda)}$$

$$D = e^{\lambda\tau} - \Gamma^2 e^{-\lambda\tau}$$

$$f^- = \frac{(2 - \lambda)}{(1 - \mu\lambda)}(1 - e^{-(1-\mu\lambda)\tau/\mu})$$

$$f^+ = \frac{(2 + \lambda)}{(1 + \mu\lambda)}(1 - e^{-(1+\mu\lambda)\tau/\mu}).$$

Here ϖ and g are the single-scattering albedo and asymmetry factor, respectively, of the scattering layer and are, of course, functions of the ice crystal size distribution and shape.

The equations above are approximate in two important respects: (i) the actual source function has been replaced by a two-stream source function, and (ii) the cloud layer has been assumed to be isothermal at a temperature T_c. Toon et al. (1977) have shown that the first approximation introduces errors in the calculated brightness temperature of less than 0.5°K. Also, the accuracy of the approximation increases as the medium in question becomes increasingly absorbing, i.e., as ϖ decreases. Since ice crystals typically exhibit fairly strong absorption ($\varpi \sim 0.5 \rightarrow 0.7$), the approximation should certainly be sufficiently accurate for our purposes. The second approximation introduces somewhat larger errors and is discussed below.

To invert Eq. (2) for the cloud optical depth, we need to determine values of the three radiances and the scattering parameters. B_e is observed by the satellite, and B_s, which is the radiance incident on the base of the cirrus cloud, is taken to be the highest radiance observed in the scene. Essentially this assumes that the surface/boundary layer emission is the same throughout the local area and that there are no underlying low to middle altitude clouds. The emission temperature of the cloud is taken to be the coldest observed brightness temperature (−78°C in this case) since this presumably represents an optically thick cloud radiating at the ambient temperature. Because an optically thinner cloud may emit radiation through a greater geometric depth, this mean temperature may be 5° or 10°C too cold in some cases. However, we shall see that this uncertainty has little impact on the derived cloud optical depth.

Obtaining τ from Eq. (2) also depends on the size and shape of the cirrus ice crystals through the dependence on ϖ and g. In this calculation we have assumed the plausible values of $\varpi = 0.5$ and $g = 0.85$ (Liou 1974). For typical theoretical crystal distributions, the asymmetry factor varies between approximately 0.72 and 0.87 (Stephens 1980); the actual value for tropical cirrus clouds is uncertain. Fortunately, for ice particles in the thermal infrared, the effect of varying g between 0.72 and 0.87 is quite small (less than 0.25°K in the calculated brightness temperature) because absorption tends to dominate any small variations in scattering. This value of the single-scattering albedo is appropriate for crystals which are large compared to the wavelength of the infrared radiation seen by the satellite (about 10 μm), but could be somewhat larger if smaller ice crystals are assumed. If the single-scattering albedo was larger, then the optical depths derived below would also be larger.

Given values of B_s and B_c, Eq. (2) can be inverted to give cirrus optical depth as a function of brightness temperature (Fig. 2). In order to illustrate the sensitivity of the inversion, calculations were carried out for surface emission temperatures of 12 and 22°C and cloud temperatures of −78° and −73°C. The curves indicate that the cloud area in Fig. 1 that has brightness temperatures between −20° and −65°C has infrared optical depths between about 1 and 3. The uncertainty in the estimated optical depths caused by an uncertainty of 10°C in the value of either the surface or cloud emission temperature is represented by the difference between the dashed and dotted curves. The uncertainty due to the surface emission temperature (the difference between the solid and dashed curves) is always relatively small. For brightness temperatures

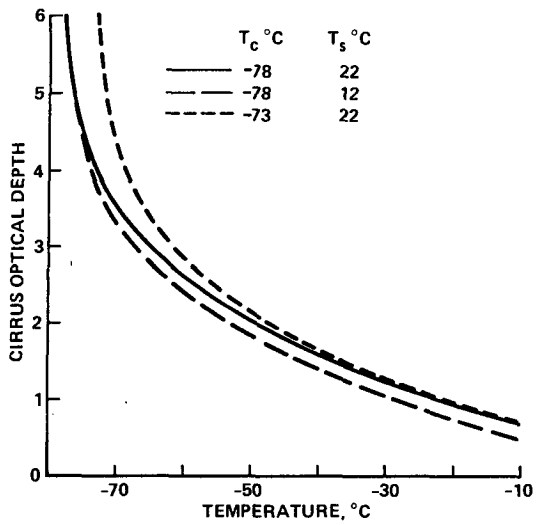

FIG. 2. Cirrus optical depth as a function of infrared brightness temperature for an isothermal cloud. Solid curve assumes a surface emission temperature of 22°C and cirrus cloud temperature of −78°C; dashed curve, a surface temperature of 12°C and cirrus temperature of −78°C; dotted curve, a surface temperature of 22°C and a cloud temperature of −73°C.

greater than about −65°C, the uncertainty in the estimated optical depth due to the uncertainty in the actual cloud temperature is on the order of 10% to 20%. At colder brightness temperatures, the estimated optical depth becomes increasingly sensitive to cloud temperature (actually, to the temperature profile in the cloud) and this simple model can no longer be used to estimate optical depth.

The relative insensitivity of the cirrus optical depth (for moderate values of the optical depth) to the values of the two emission temperatures is the result of the large difference between near-surface and near-tropopause temperatures in the tropics. Because the temperature difference is so great, the 10 μm emission at the surface temperature is almost a factor of 10 times larger than the emission at the tropopause temperature. By comparison, varying the emission temperature of either the surface or the cloud by 5° to 10°K only changes the broad-band emission by 10% to 15%. Thus, the important parameter in the inversion is the layer optical depth since it controls the mixture of "warm" surface radiation and "cold" cloud radiation that together produce the measured brightness temperature. At large optical depths, the brightness temperature is dominated by emission from the cloud and the results become sensitive to the actual thermal structure within the cloud; hence, our simple model no longer applies. Evidence of this increased sensitivity is seen in the increasing slope of the curves in Fig. 2 at colder temperatures.

As we discuss in the following section, the specific extinction for the ice crystals in this anvil is on the order of 0.033 $m^2\ g^{-1}$. Thus, optical depths between 1 and 3 imply column ice concentrations of 30 to 90 $g\ m^{-2}$. Aircraft and radiosonde measurements of the temperature profile (see Fig. 3) in the anvil outflow suggest an anvil layer approximately 2 km thick. If we assume an average anvil thickness on the order of 2 km, then the average ice water content in the anvil is about 0.015 to 0.045 $g\ m^{-3}$. It should be emphasized that this is only a rough estimate of the likely ice water content. Because we have only inferential information on the actual geometric thickness of the anvil, and because we lack precise information on the crystal size and shape, the ice water content is probably uncertain to within a factor of 2 to 5.

In summary, anvils of the type shown in the infrared image in Fig. 1 are optically thick in the central region and must have optical depths of at least 2 within a kilometer or two of the tropopause. The region in the image surrounding the core where the observed brightness temperature is on the order of −50° probably corresponds to cloud with an optical depth of about 1 to 3. The ice water content in this region averages approximately 0.03 $g\ m^{-3}$. While this number has considerable uncertainty attached to it, it cannot be much less than about 0.005 $g\ m^{-3}$ without implying anvils which are far too thick geometrically. Likewise, the ice water content cannot be much greater than about 0.1 $g\ m^{-3}$ without implying anvils which are too thin to

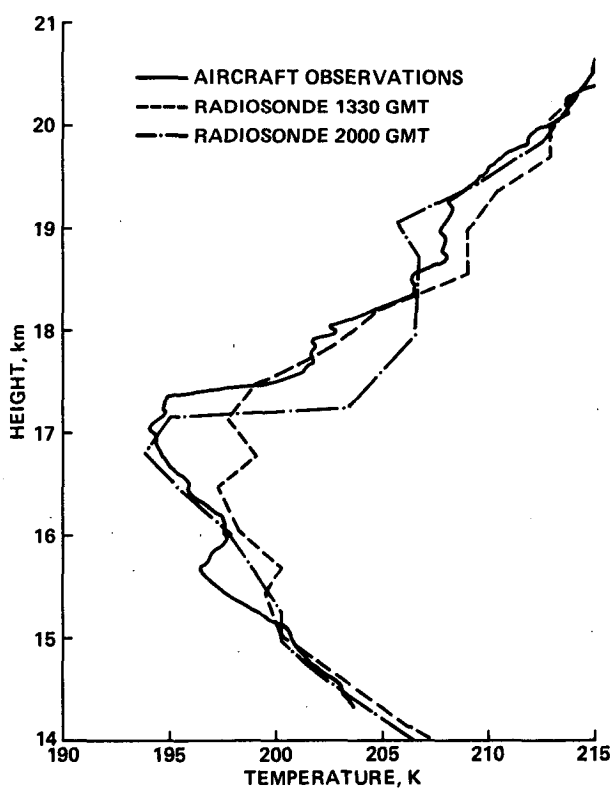

FIG. 3. Temperature profile near the tropopause as measured by aircraft (solid curve) and by radiosonde at 1330 UTC (dash) and at 2000 UTC (chain).

be sustained against diffusive processes. The exception to this last statement is in the center of the anvil where the very cold brightness temperatures do suggest a high ice water content probably at the top of the deep convective towers.

3. Data

From the infrared satellite image we were able to infer infrared optical depths and approximate values of the cloud top temperature and an average IWC. More precise values of some of the environmental and cirrus cloud parameters needed for model studies were obtained from observations of this anvil system taken from the NASA U-2 aircraft during Flight 7 (12 September 1980) of the 1980 Stratospheric Tropospheric Exchange Experiment carried out near Panama (Margozzi 1983) and from radiosondes over Panama. On this day the aircraft flew over and penetrated into the large and fairly uniform anvil shown in Fig. 1. The actual flight track and anvil penetration areas are depicted in Fig. 1b and identified in the legend. During the flight, measurements of temperature, total water concentration, and ice crystal size distribution were made. Unfortunately, due to flight limitations, the U-2 was not able to penetrate deeply into the anvil and produce vertical profiles of the various parameters. Thus, we are forced to extrapolate from the values at anvil top to get complete vertical distributions. Since these extrapolations can be carried out in a number of ways, sensitivity tests were performed and are discussed in subsequent sections.

In Fig. 3, an aircraft temperature profile (measured with a Rosemount probe) obtained at approximately 1520 UTC is compared in the vicinity of the tropopause with two radiosonde profiles acquired at 1330 and 2000 UTC at the airbase indicated in Fig. 1b. The profile at 1330 UTC is quantitatively similar to the average temperature sounding in the Panama region during the entire experiment and may be taken to be representative of typical environmental conditions. The aircraft profile was taken during final descent of the aircraft, just off the downwind edge of the anvil. Note the substantially cooler layer in the region between 15 and 17 km. Although no ice crystals were reported on descent through this layer, the water vapor measurements made with a Lyman-α hygrometer (Kley et al. 1983) show high values of the mixing ratio, some at saturation, associated with it. Since the air in the upper troposphere is on average below saturation, this saturated layer suggests that this air is flowing out of the anvil and thus may be representative of air which has been modified by deep convection and processing in the anvil. The 2000 UTC sounding was acquired several hours later directly downwind from the anvil. It exhibits a strong correlation with the aircraft sounding below about 17 km, suggesting that the layer of cold air produced by the convective system is being advected downwind.

While it is tempting to assume that the aircraft descent profile in Fig. 3 is equivalent to the in-cloud temperature, caution must be exercised. Measurements of actual cloud top temperatures made when the U-2 penetrated the anvil show considerable variability, in part because during penetration the aircraft follows a roughly parabolic flight path that results in considerable horizontal, as well as vertical, variations. In his analysis of these aircraft data, Danielsen (1982b) produced a composite temperature profile by plotting all the U-2 temperature measurements made in the vicinity of the anvil as a function of aircraft altitude. The minimum temperature in this composite profile is about 190 K, although temperatures at least 5°K warmer were also measured at the same altitude. Danielsen then concluded that the cloud top temperature is represented by the minimum temperature of 190 K, which is about 4°K colder than the aircraft descent profile at this same altitude. Furthermore, he argued that the temperature profile in the cirrus anvil was adiabatic, initially due to mixing and subsequently due to radiative destabilization. The aircraft and 2000Z profiles are inconsistent with this interpretation, suggesting that they are not indicative of actual in-cloud temperatures. Since Danielsen's technique ignores spatial inhomogeneities and since no aircraft descent was made through the anvil, the actual in-cloud profile remains in doubt.

Because we do not have sufficient data to resolve this problem, we chose to treat the in-cloud temperature profile as a parameter. We used the 1330Z radiosonde profile to define the environment below cloud base and above cloud top, the latter being fixed in these calculations at 17 km. Cloud base temperature was determined from the environmental sounding and the in-cloud temperature gradient was varied from adiabatic (-10°K km^{-1}), to an intermediate gradient consistent with the profiles in Fig. 3 (-3°K km^{-1}), to isothermal. These profiles are similar to those in Fig. 3 in that the temperature profile is continuous at cloud bottom but may have a sharp discontinuity at cloud top (17 km). In addition, some calculations were carried out with a "Z" shaped temperature profile adapted from Danielsen's (1982b) Fig. 2a and 2b. For this case, the temperature at the cloud midpoint was set equal to the environmental temperature at cloud base while an adiabatic lapse rate was imposed on the anvil. The resulting temperature profile has a sharp discontinuity at cloud bottom as well as cloud top.

The measurements of total water and of the size distribution of the ice crystals in the anvil taken during this same flight both suggest an IWC of about 0.02 g m^{-3} in the top few hundred meters of the anvil (Knollenberg et al. 1982, 1983; Kley et al. 1982, 1983). The size distribution measurements were made with a 2-D imaging probe and integrated to produce IWC. Since the 2-D probe does not resolve particles smaller than about 20 μm diameter, these values of IWC may be somewhat underestimated. However, the measured

value of IWC is consistent with the values inferred above from the infrared satellite imagery. Because measurements could not be obtained throughout the anvil, the variation of IWC with depth is uncertain. Therefore, we have carried out calculations for several different assumed IWC profiles: (i) constant with altitude, (ii) decreasing linearly from cloud base, and (iii) parabolic with a maximum at the cloud midpoint and minima at both cloud boundaries. Since, from a radiative point of view, the most important property of a cloud is its optical thickness, we generally kept the total optical depth fixed while varying the IWC profile. This results in a small inconsistency because the IWC at cloud top then is allowed to vary rather than be fixed by the measurements. However, this inconsistency is offset by the easier intercomparison of model calculations for identical optical thicknesses.

The ice extinction and scattering coefficients needed for the multiple scattering code were computed from Mie theory assuming a lognormal distribution of spheres with a volume mean radius of 50 μm and standard deviation of 1.3. While these values were obtained from the Panama measurements (Knollenberg et al. 1982, 1983), there is substantial uncertainty attached to them due to the limited number of observations, the lack of deep penetration into the anvil, and the difficulty of interpreting the measurements for ice crystals. In addition, error is introduced by the use of spheres, rather than some crystal shape. Since we have only minimal information on ice crystal shape for these clouds and the information which we do have (Knollenberg et al. 1983) indicates highly irregular crystal shapes, we felt that it was premature to investigate detailed distributions of crystal shapes. Furthermore, because we are interested primarily in infrared fluxes, the error introduced by the use of spheres is small. We have carried out calculations of equal cross-sectional area spheres and hexagons and find that the difference in single-scattering albedo at infrared wavelengths (where appreciable absorption occurs, $\varpi \sim 0.5$–0.8) is less than 10%. For very small optical depths where multiple scattering can be neglected, the difference in the flux is directly proportional to the difference in the single-scattering albedo. As multiple scattering effects become important, the difference in the flux decreases and essentially disappears at optical depths of a few. Regardless of the optical depth, the errors introduced by use of spheres is dwarfed by the uncertainties in the other cloud parameters such as ice water content. Irregular particle shape tends to have a much greater effect on the scattered phase function (and consequently on the asymmetry factor), which becomes important at large values of the single-scattering albedo. Therefore, our use of spheres has a fairly negligible effect on the results of the infrared calculations, but may have some impact on our calculations of reflected and absorbed solar radiation.

The lack of probe resolution for particles less than 20 μm diameter introduces a potentially greater error. If large numbers of these smaller particles were present, they would not only increase the optical depth substantially while producing only a modest increment in IWC, but also increase the single-scattering albedo, which would produce more scattering and less absorption per unit mass, particularly at infrared wavelengths. Without more detailed measurements, we cannot determine the amount of smaller particles, if any, and therefore have not included them in our model calculations. We have attempted to circumvent this problem by expressing our results in terms of optical depth, which includes both number of particles and extinction efficiency. Thus, to some extent, the results can be scaled to different particle distributions if the appropriate mass extinction factor is known. We intend to utilize the data obtained in STEP to further investigate this problem.

Refractive indices of ice at the various wavelengths were obtained from Warren (1984). For reference, we calculate a specific extinction of 0.0315 $m^2 g^{-1}$ at 0.55 μm and 0.0333 $m^2 g^{-1}$ at 11.3 μm. It is possible, and perhaps likely, that the ice crystal size distribution varies with depth in the anvil which, in turn, would produce variations in the specific extinction and the optical depth. Since no data is available on variations in the size distribution, we have elected to hold the size constant and vary only the assumed optical depth.

Based on the change in lapse rate occurring at about 15 km shown in the measured profiles in Fig. 3, the anvil depth was initially set to 2 km. For a constant IWC of 0.02 g m^{-3}, this gives optical depths of 1.26 at a wavelength of 0.55 and 1.33 at 11 μm. From Fig. 2, a brightness temperature of about -30°C can be inferred. In the following sections, this cloud with an in-cloud lapse rate of -3°K km^{-1} will be referred to as the standard anvil and will serve as a reference for comparisons.

4. Model description

In order to investigate in more detail the radiative effects of cirrus clouds, a series of calculations were performed using two infrared radiative transfer models. The first, which was used for the in-cloud infrared radiative transfer studies, is a modified version of the model described by Pollack and McKay (1985). Emission and scattering of infrared radiation within the cirrus cloud are treated with a multilayer, two-stream algorithm which subdivides the cloud into at least ten layers, each of which has homogeneous cloud properties. Temperatures at layer boundaries are specified by imposing a constant lapse rate throughout the cloud. Within each layer, an analytic solution to the radiative transfer equation is obtained by expanding the Planck function as a linear function of optical depth constrained by the values at the layer boundaries. Given that our typical layer thickness is 200 m and that the

maximum variation in temperature across this layer is about 2°K under the assumption of an adiabatic lapse rate, this expansion is quite accurate.

To resolve spectral variations, the infrared spectrum from 4.5 to 250 μm is divided into 34 intervals. In each interval, the gaseous transmittance due to H_2O, CO_2 and O_3 is computed from absorption line data and then fit using exponential sums. The pressure dependence of the equivalent absorption coefficients is computed assuming a power-law (i.e., $k_i \propto p^n$) where n varies with gas species. While water vapor continuum absorption and its overlap with the CO_2 15 μm absorption is treated explicitly, the H_2O and CO_2 band overlap in the vicinity of 20 μm is not considered. Details of the spectral intervals and absorption coefficients used in the model are given in Table 1 of Pollack and McKay (1985). The upwelling flux at cloud bottom is computed using a formulation of the two-stream solution which neglects scattering in the subcloud atmosphere. The downwelling flux at cloud top, which is fairly negligible for cloud tops at 17 km, is calculated from a simple scale-height approximation based on climatological distributions of the gaseous absorbers.

For most of the calculations the layer thickness was set to 200 m. Because the two-stream solution is analytic, heating rates can in principle be evaluated at a resolution much finer than that defined by the layer thicknesses. However, since the temperature profile is defined at the layer boundaries and absorber amounts are calculated per layer, evaluation of the heating rates at higher resolution is inconsistent with the specified input information. Therefore, in the following discussion and figures, the given heating rates are layer averages. While it could be argued that this underestimates the actual values at cloud boundaries, it should be noted that in reality we are unlikely to be able to measure cloud boundaries or radiative divergences on scales much less than a few hundred meters.

While this first model has the advantages of being computationally efficient and accurate within the cirrus cloud, it was not designed to calculate fluxes or heating rates in the environment surrounding the cloud. A second model based on the adding method and including internal emission was used to compute environmental heating rates. In this model, 12 spectral intervals are used. As with the first model, the transmittance for each interval is derived from absorption line data for O_3, CO_2 and H_2O and then fit with a weighted exponential sum. The vertical resolution of this model is 1 km and the model domain extends from the surface to 30 km.

Solar heating rates were computed using a multilevel, δ4-stream model which we have used in several previous studies (Pollack and Ackerman 1983; Ackerman and Valero 1984). This model has 26 spectral intervals covering the region from 0.25 to 4.5 μm. Eight intervals are considered free of gaseous absorption. In the remaining intervals, absorption due to O_2, O_3, CO_2 and H_2O is treated using pressure-dependent exponential sum fits to laboratory data. As in the infrared model, the absorption coefficients were assumed to have a power-law dependence on pressure where the pressure exponent varied with gas species. In this model, the overlapping H_2O and CO_2 bands in the near infrared are treated explicitly assuming random overlap, i.e., the two exponential sums are multiplied together and calculations are carried out for all combinations of absorption coefficients. Rayleigh scatter is included at all wavelengths, as is scattering and absorption due to ice crystals. For the calculations reported here, the model was run for 20 to 25 layers covering the region from the surface to 30 km. Typical in-cloud resolution was 200 m. In all cases, the underlying surface was assumed to be tropical ocean with a spectrally invarient albedo of 0.05.

5. Infrared heating rates

a. Variations in the in-cloud temperature profile

The influence of the in-cloud temperature profile on infrared heating rates in the cirrus anvil is shown in Fig. 4, where the four profiles described in the preceding section were used. Since the adiabatic, aircraft, and isothermal profiles all have the same cloud base temperature, they have nearly identical cloud base heating rates. The difference in cloud-top heating rate results from the different cloud-top temperatures. The cloud top is coldest for an assumed adiabatic lapse rate; therefore it radiates less for a fixed emissivity leading to a larger net heating at cloud top. The "Z" profile is warmer at cloud bottom than any of the other profiles, so the cloud base radiates more effectively and thus heats less. The largest difference in heating rates occurs at cloud top and is on the order of 12°K day^{-1}. By comparison with the heating rate differences produced in some of the cases below, this difference is relatively small.

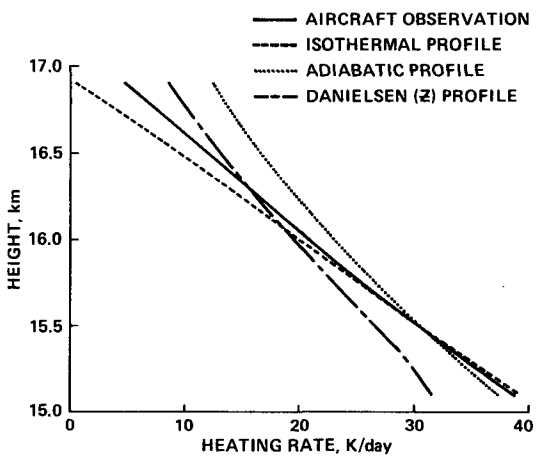

FIG. 4. In-cloud heating rates as a function of height for four lapse rates: isothermal (dashed curve), measured by aircraft (solid), adiabatic (dotted), and Danielsen's "Z" curve (chain).

Perhaps the most interesting aspect of the results shown in Fig. 4 is that the cloud is heated at all levels including the top. A similar point was made by Platt et al. (1984) based on calculations in which cirrus clouds were treated as grey-body absorbers. While such behavior is perhaps counter-intuitive, it is readily understood from simple radiative theory. Because of the warm tropical ocean and boundary layer, a large infrared flux is incident on the cloud bottom. Since the cloud has an absorption optical depth of only about 0.6 at wavelengths in the window region (8 to 13 μm), this warm radiation is absorbed throughout the entire vertical extent of the cloud. Cloud temperatures, on the other hand, range from 200 to 180 K; hence, the emission by the cloud elements is small and shifted towards longer, and more opaque, wavelengths which limits the cloud-top cooling.

This point is further illustrated in Fig. 5 where the flux divergence across the cloud layer (defined as $-\Delta F_\nu/\Delta z$ where F_ν is the net flux at wavelength ν) is plotted as a function of wavenumber for both the standard cloud and no cloud. The average heating rate in the layer is directly proportional to this quantity. For the no-cloud case, a small amount of heating occurs in the CO_2 15 μm band due to radiative exchange of the cold tropopause layer with the warmer layers above and below. A slight cooling is evident at the very longest wavelengths due to emission in the water vapor rotation bands. When the cirrus cloud is introduced into the layer, the picture changes dramatically. Very strong heating occurs in the window region and in the small spectral gap at about 500 cm^{-1} between the 15 μm band and the water rotation band. At these wavelengths the warm radiation incident on the cloud from the troposphere exceeds the radiation which can be emitted by the cold layer. However, the layer cools at far infrared wavelengths because, due to the temperature dependence of blackbody emission, the emission from the cold cloud ($T \approx 200$ K) is much greater than the emission from the warmer troposphere at long wavelengths. While this plot of the spectral flux divergence supports the notion that cirrus clouds have their dominant influence on window radiation and, therefore, computational models need only include window effects (e.g., Ramaswamy and Detwiler 1986), it also introduces a cautionary note that important effects can occur in the wings of the vibration band, in the CO_2–H_2O overlap, and in the far-infrared. Figure 5 also shows that on the average the cloud layer is heating. Total layer heating for the cases shown in Fig. 4 is about 22°K day^{-1} and is greatest for the coldest temperature profile.

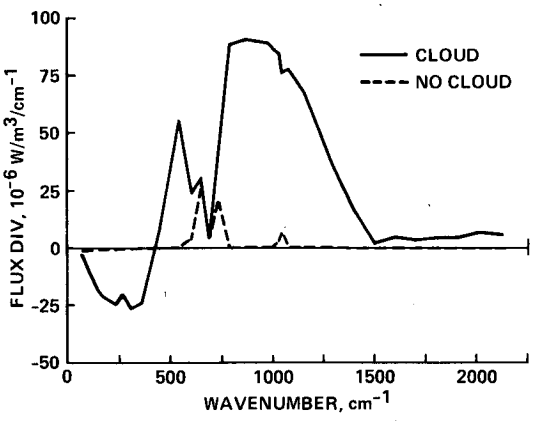

FIG. 5. Flux divergence (in units of -10^6 W m^{-3} cm^{-1}) across the layer between 15 and 17 km as a function of wavenumber. Solid curve is for standard cloud case, dash for no-cloud. Note that positive ordinate values imply heating and negative values imply cooling.

The vertical gradient of the heating rate within the anvil and the net layer heating have several interesting implications for the anvil and for its interaction with the surrounding environment. In his proposed dehydration mechanism, Danielsen (1982b) hypothesized that, as a result of mixing during formation, anvil layers initially have a near-adiabatic temperature profile and that this instability is maintained by infrared radiative transfer. These calculations support this hypothesis to the extent that the vertical gradients in the heating rates in Fig. 4 are clearly sufficient to maintain turbulent mixing in an adiabatic layer. However, if the anvil temperature profile is not initially adiabatic, the timescale needed to achieve destabilization by radiative heating may be long compared to that of other processes which can affect the anvil. For instance, if the anvil initially has a lapse rate of about -3°K km^{-1} (the aircraft descent profile observed in the Panama data) and the differential heating between cloud top and bottom is about 1.4°K h^{-1}, then it will take on the order of half a day for the anvil to become convectively unstable.

b. Variations in IWC amount and distribution

In addition to the dependence on lapse rate, the calculated heating rate profiles shown in Fig. 4 depend on the assumed values of several other cloud parameters such as IWC, particle size, and cloud vertical extent. As noted above, because the effects of IWC and particle size are strongly intertwined through their impact on cloud optical depth, we have chosen to simplify the analysis by only considering variations in IWC. Shown in Fig. 6 are curves for constant IWCs of 0.02 g m^{-3}, 0.002 g m^{-3} and 0.1 g m^{-3}. On the basis of the analysis of the infrared satellite data presented above, an IWC of 0.1 g m^{-3} represents a high but plausible value. An IWC of 0.002 would correspond to a fairly tenuous anvil at the limits of visibility. This range of IWC is fairly large but, given the lack of IWC observations in high, cold anvils, it is difficult to reduce it substantially. Also, for this and subsequent calculations, we have used the aircraft temperature profile to define the in-cloud environment (see Fig. 3).

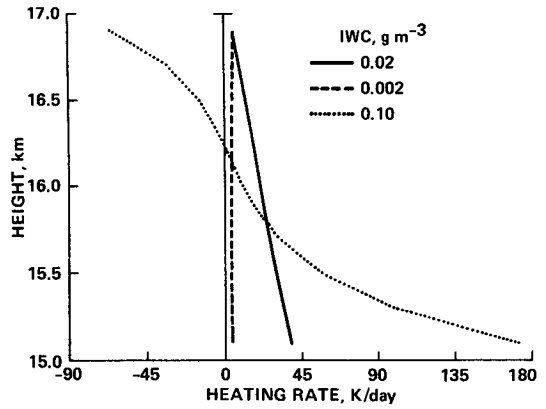

FIG. 6. In-cloud heating rates as a function of height for three constant ice water contents: 0.02 g m^{-3} (solid curve), 0.002 g m^{-3} (dashed), and 0.10 g m^{-3} (dotted). (Note the horizontal scale of this figure is substantially compressed relative to other figures.)

At the largest value of IWC (0.1 g m^{-3}), the cloud has an optical depth of about 6.7 at 11 μm. At this optical thickness, the cloud experiences strong radiative heating at cloud base and cooling at cloud top with differential heating rates between cloud bottom and top in excess of 200°K day^{-1}. The average heating rate for the entire anvil layer, however, is only about 30°K day^{-1}, which is approximately 35% greater than for the cloud with an IWC of 0.02 g m^{-3}. These results are consistent with the heating rates calculated by Platt et al. (1984) for a cirrus cloud with an approximate optical depth of 3.2 at 11 μm (which would correspond roughly to an average IWC of 0.05 g m^{-3} for a cloud with a vertical extent of 2 km). Although their model cloud (located between 14.5 and 16 km) was slightly lower in altitude and geometrically thinner than ours, their calculated net heating of about 25° to 35°K day^{-1} and differential heating rate of about 100°K day^{-1} agrees well with our results. Such large heating rate gradients would likely result in strong convective mixing of the layer. They might also have a considerable effect on cloud microphysics. Platt et al. (1984) state that the amount of heating which they calculate, if used entirely for evaporation, could evaporate the cloud within about ten minutes. However, they also note that anvil dissipation times are much longer than this (about two hours for the one case that they observed) which suggests that much of the radiative heating results in layer heating.

Increasing the total IWC (and hence the optical depth) of the anvil also has a fairly dramatic effect on the outgoing longwave radiation. For example, the outgoing radiation for the very thin cirrus (IWC of 0.002 g m^{-3}) is 273 W m^{-2}, which is slightly less than the clear sky radiance of 297 W m^{-2}. For IWC of 0.02 g m^{-3}, the outgoing radiation at cloud top is 149 W m^{-2}, while for IWC of 0.10 g m^{-3}, the outgoing radiation is 81 W m^{-2}. Thus, as the anvil optical depth increases, infrared radiation loss from the planet is reduced until the anvil becomes optically thick.

These values of infrared emittance are quite consistent with satellite observations. For example, ERBE observations over the western Pacific in the vicinity of the Phillipine Sea (ERBE Science Team 1986) show maximum infrared emittances on the order of 290 to 310 W m^{-2}. In the same scene, two hurricanes are evident, both with infrared emittances less than 75 W m^{-2} at their centers. Since 75 W m^{-2} corresponds to a broadband brightness temperature of 190 K, one can infer that these hurricanes have high optical depths near the tropopause. This in turn implies IWC's on the order of or greater than 0.10 g m^{-3} given ice crystal distributions similar to those assumed in this study.

The effect of increasing optical depth on the outgoing IR radiance is further illustrated in Fig. 7 where the upward radiance at 10 μm at cloud top is plotted as a function of anvil optical depth and emission angle measured from the zenith. For ease of interpretation, the radiance is given as brightness temperature. The calculations were carried out using an infrared adding–doubling code. The anvil was assumed to have a single-scattering albedo of 0.5, an asymmetry factor of 0.86, a Henyey–Greenstein phase function, a cloud-base temperature of 200 K, and a lapse rate of −3°K km^{-1}. The bottom boundary condition was an isotropic radiation field at an equivalent blackbody temperature of 296.5 K, which was computed from the Panama soundings discussed above. The wavelength was chosen as representative of the infrared window channels used on meteorological satellites. It is apparent that the upwelling radiance is extremely sensitive to optical depths in the range of 0.5 to 5.0. For instance, increasing the optical depth from 1 to 3 can decrease the brightness temperature by about 50°K. Not surprisingly, the radiance exhibits the greatest sensitivity to emission angle at these same values of the optical depth.

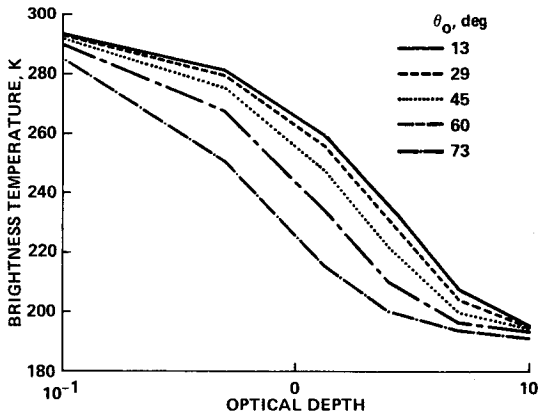

FIG. 7. The 10 μm brightness temperature for a cirrus anvil as a function of optical depth. The curves from uppermost to lowermost are for values of the viewing angle of 13°, 29°, 45°, 60° and 73°, respectively.

The preceding calculations have assumed that the IWC is constant with altitude within the cloud. However, this is not necessarily the case. In Fig. 8, heating rate profiles are shown for three possible profiles of IWC: constant with altitude, linearly decreasing with altitude, and parabolic about the cloud midpoint. In each case, the total optical depth has been held fixed while the in-cloud distribution has been modified. Not unexpectedly, the linearly varying profile redistributes the heating towards cloud bottom. The parabolic distribution produces a heating rate profile that is peaked broadly somewhat below the IWC maximum.

Since the linearly varying profile produces about the same net layer heating but with a stronger vertical gradient of the heating, it would probably produce the same turbulent response in the anvil as the constant IWC heating rates. However, the large heating rates at cloud bottom may be significant for cloud microphysical processes. The parabolic distribution might tend to reduce turbulence and mixing since the maximum heating occurs near the middle of the cloud rather than at cloud bottom. Again, the interactions among radiation, turbulence, and cloud microphysics need to be explored with a coupled model.

c. *Variations in cloud thickness*

The effect of increasing cloud thickness is shown in Fig. 9. In these calculations, we have held constant both cloud top (at 17 km) and IWC (at 0.02 g m^{-3}) while extending the cloud bottom down to 7 km in increments of two kilometers. As expected, the cloud top heating decreases (eventually becoming cooling) as the cloud extent increases because the corresponding increase in optical depth prevents the warm surface radiation from penetrating to cloud top. As the cloud becomes optically thick, the cloud top cooling asymptotically approaches a value independent of cloud extent but dependent on the IWC.

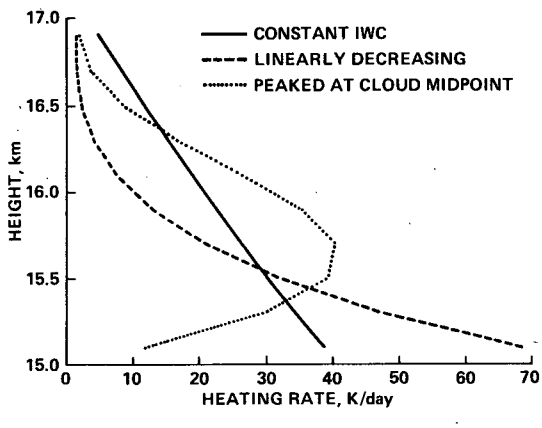

FIG. 8. In-cloud heating rates as a function of height for three IWC profiles all with the same optical depth: constant with altitude (solid curve), linearly decreasing with altitude (dashed), and peaked at cloud midpoint (dotted).

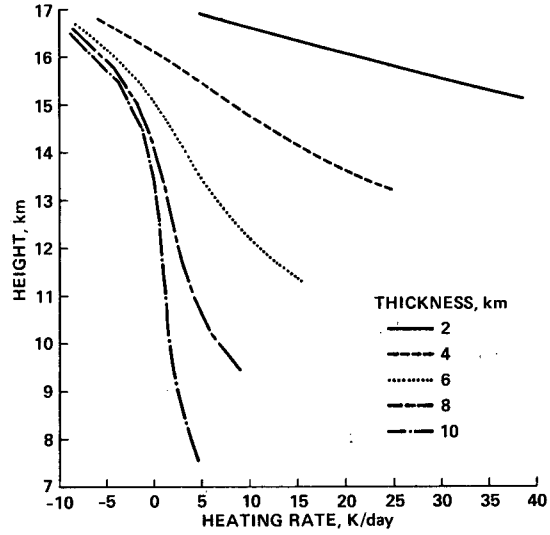

FIG. 9. In-cloud heating rates as a function of height for clouds with a constant IWC and geometric thicknesses ranging from 2 to 10 km. In all cases, cloud top is at 17 km.

The cloud base warming also decreases but at a greater rate. This is primarily due to warmer cloud bottom temperatures as the cloud is extended downwards, but also to a greater heat capacity per unit volume at lower altitudes since the air is more dense. This latter effect could be counterbalanced and the heating increased somewhat if the IWC was assumed to have a constant mixing ratio rather than a constant mass per unit volume. As a consequence of the relatively greater reduction in cloud base heating, the radiational destabilization is *reduced,* rather than enhanced, as the cloud is extended. Thus, deep anvil systems such as those encountered during Winter Monex probably are less turbulent than high, thin anvils. In addition, the total layer heating is reduced to values of only 1.0° to 2.5°K day^{-1} for 8 to 10 km deep clouds.

An additional point of interest is that the emitted infrared radiation at 10 μm for both the 8 and 10 km clouds corresponds to a brightness temperature of 207 K or −66°C. This is about 12°C warmer than the actual cloud top temperature, which indicates that the outgoing infrared emission originates within the top two kilometers or so of the cloud. By comparison the coldest temperatures in Fig. 1 are less than −77°C, which indicates emission originating right at the tropopause. From this, we can conclude that, given the particle distribution used in this study, an IWC of 0.02 g m^{-3} is inconsistent with the coldest temperatures seen in the satellite image regardless of the geometric thickness of the underlying clouds. In order to produce the requisite optical depth close to the tropopause, the IWC must be on the order of 0.1 g m^{-3}. If smaller particles than those assumed here were present, then a smaller IWC would produce the necessary optical depth. Since the 2-D imaging probe flown in the Panama experiment

(Knollenberg et al. 1982) does not measure particle sizes below 40 μm diameter, it is possible that smaller particles were present and did contribute significantly to the optical depth. Resolution of this uncertainty must await further observations.

d. Variations in lower boundary condition

As noted above, the vertical distribution of heating within the cloud is also dependent on the radiation incident on the cloud from below. In the preceding cases, we assumed that the atmosphere below the cloud was clear. However, it is possible that low-level clouds are present underneath and adjacent to anvils. In the case of mesoscale cloud clusters, it is also possible that anvil layers could form overtop of the cloud cluster. To simulate these conditions, we have replaced the 300 K ocean surface first with a black surface at 5 km (temperature of 273 K), and then with a black surface at 10 km (temperature of 240 K). The resulting heating rate profiles are compared in Fig. 10. As the upwelling radiation originates at increasingly higher and colder levels, the total heating in the layer decreases. In addition, the vertical gradient of the heating decreases thereby reducing the radiative destabilization. In the limit as the black surface is raised to cloud base, the resulting heating rates tend to resemble those shown for the deep clouds in Fig. 9.

e. Effect on atmospheric heating rates

In the preceding discussion we have concentrated on heating rates within the anvil itself. However, we have also noted that the presence of an anvil can strongly modify the infrared radiation field. This in turn will affect atmospheric heating rates. To investigate the magnitude of this effect, we have computed the infrared heating rates for 1 km thick layers from the ground to 30 km in the presence of an anvil between 15 and 17 km. Temperature, water vapor, and ozone profiles for the calculations were obtained from radiosonde ascents taken during the Panama experiment (Margozzi 1983). In this case, the anvil is divided only into two layers and constant IWCs of 0.002, 0.02, 0.06 and 0.1 g m^{-3} were used. The resulting heating rate profiles are shown in Fig. 11.

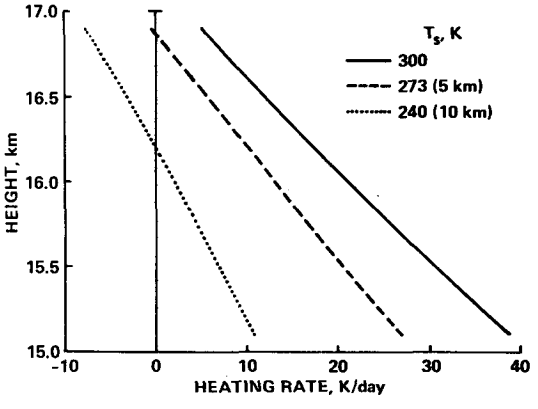

FIG. 10. In-cloud heating rates as a function of height for a cloud subject to upwelling radiation from a clear atmosphere (solid curve), from a 273 K black surface at 5 km (dashed), and from a 240 K black surface at 10 km (dotted).

In the clear atmosphere case, the lower stratosphere from about 17 to 23 km is heating on the order of 1°K day^{-1}, primarily due to ozone absorption. When the anvils are present, the heating rate is suppressed and, for the more optically thick anvils, cooling of about 1.5°K day^{-1} occurs in this region. As expected, the anvils suppress cooling from the middle troposphere below the cloud. Similar results were obtained by Doherty et al. (1984) for an optically thick anvil placed between 14 and 16 km in a January-mean Darwin sounding. They also point out that nearly equivalent coolings can be produced by decreasing the ozone concentration in the lower stratosphere, which might be expected to occur due to general ascent of tropical tropospheric air in the vicinity of Micronesia (the so-called "stratospheric fountain" effect, Newell and Gould-Stewart 1981).

6. Solar heating rates

Since ice is basically transparent at wavelengths shortward of 2 μm, there is a tendency to ignore solar heating. However, ice has a very pronounced absorption feature in the vicinity of 3 μm that can lead to significant heating, particularly in the tropics where the incident solar radiation is quite large. To illustrate this effect, instantaneous solar heating rates for a clear sky and for 2 km thick anvils with constant IWCs of 0.002, 0.02, 0.06 and 0.1 g m^{-3} are shown in Fig. 12. In the calculations, the cosine of the solar zenith angle ($\cos\theta_0$) was set to 0.60, which is the annual average value at 5° latitude (Paltridge and Platt 1976), and the surface albedo to 0.05, which is appropriate for ocean surfaces. For the standard cloud (dotted line), the heating rate is on the order of 6°K day^{-1} throughout the cloud. For larger IWCs, the heating rate profile becomes noticeable skewed towards cloud top and reaches values on the order of 20° to 40°K day^{-1}.

These solar heating rate computations bring out several interesting points. First, and obviously, solar radiation heats the cloud layer. The average heating rate is 6.3°K day^{-1} for a constant IWC of 0.02 g m^{-3} and 18°K day^{-1} for an IWC of 0.1 g m^{-3}. Second, the solar heating peaks at cloud top and, thereby, partially compensates the tendency of the IR to preferentially heat the cloud bottom. The compensation becomes more pronounced for greater IWCs due to the exponential nature of the solar absorption. Third, the importance of the solar heating relative to the infrared heating increases with increasing IWC. For example, the average infrared heating is about 22°K day^{-1} for a cloud with an IWC of 0.02 g m^{-3} and about 32°K

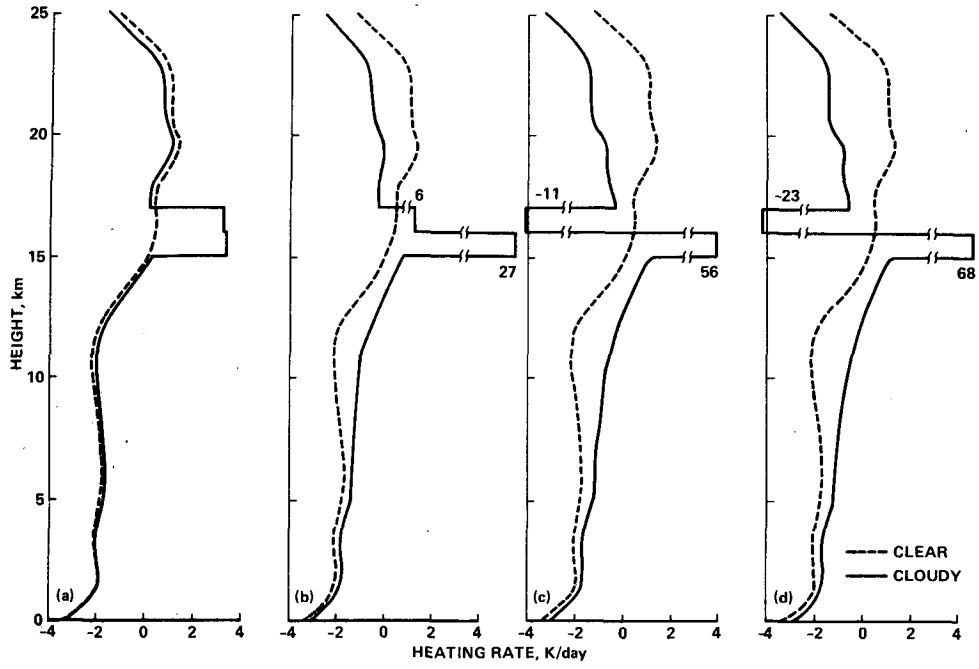

FIG. 11. Infrared heating rate profiles for a clear atmosphere (dashed curves) and for atmospheres containing cirrus anvils (solid curves). Curves are shown for anvils with IWCs of (a) 0.002, (b) 0.02, (c) 0.06, and (d) 0.1 g m^{-3}. Note that the heating rates in the anvil itself in cases (b)–(d) are not plotted to scale. The numbers indicate the average heating rates in the top and bottom anvil layers.

day^{-1} for an IWC of 0.1 g m^{-3}. Thus for the first cloud, the solar heating is 29% of the IR heating, while for the second it is 56%. From these points we conclude that solar heating of anvils may be an important factor, particularly in the case of deep anvils or anvils with high IWCs. The heating will tend to stabilize the anvil against convection while also increasing the average layer temperature.

The diurnal variations of the solar heating should also be mentioned. For our standard cloud, the solar heating is relatively insensitive to zenith angle for $\theta_0 \leq 65°$. However, for clouds with larger IWCs, both the heating rate profile and the total solar heating vary substantially with solar zenith angle. Since the lifetime of these anvil systems often exceeds several hours, these variations in solar heating may be important in the anvil evolution. For instance, Minnis and Harrison (1984) found a small but statistically significant diurnal variation in high cloudiness over tropical oceanic regions. While the formation of high clouds is probably largely controlled by deep convection, their persistence may be strongly influenced by radiational heating. In their modeling of midlatitude cirrus decks, Starr and Cox (1985b) found that radiative heating affected the structure and bulk properties of the simulated cirrus, including the fact that midday cirrus were less dense overall than nocturnal cirrus. Since the radiative forcing is stronger in tropical cirrus, we would expect the effects on structure and IWC to be even larger.

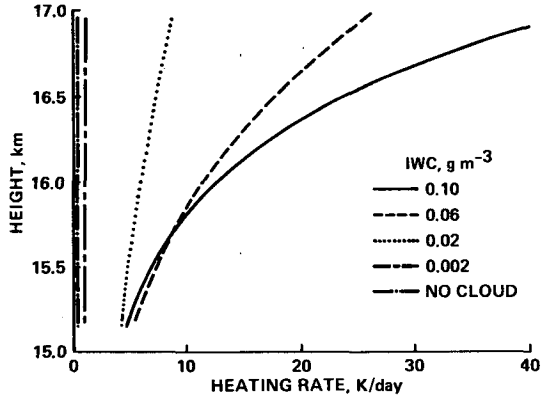

FIG. 12. Solar heating rates as a function of height for clear sky and for IWCs of 0.002, 0.02, 0.06 and 0.1 g m^{-3}. The solar zenith angle is 53°.

7. Dynamical implications

The dynamical importance of the calculated heating rates within the anvils lies both in the strong vertical gradients and in the integrated net heating of the entire cloud. If an adiabatic profile has been produced by mechanically-generated turbulence, the heating gradients will maintain the adiabatic profile by convective turbulent mixing. This mixing will tend to distribute

the vertically-varying heating uniformly throughout the system allowing us, as a first approximation, to view the anvil as a quasi-uniform parcel that responds as a unit to the anvil-averaged heating of about 30°K day^{-1} (including solar heating). Ignoring horizontal advection, the temperature of the anvil's center of mass can be described by

$$\frac{R}{H}\frac{\partial T}{\partial t} + N^2 w = \frac{RQ}{H}. \tag{5}$$

Here N is the Brunt–Väisälä frequency ($\sim$0.02 s^{-1}), H the atmospheric scale height ($\sim$6 km), Q the vertically-averaged heating rate over the anvil, R the gas constant, T the local temperature, and w the local vertical velocity. This equation describes temperature and vertical velocity both within and outside the anvil at the altitude of the anvil's center of mass but outside the anvil Q is simply set to zero.

From Eq. (5), it is clear that the heating will be balanced either by local temperature change [$(R/H)\partial T/\partial t$], by vertical motion ($N^2 w$), or by some combination. In the limiting case where the environmental temperature at the anvil altitude is unchanged, the first term vanishes, and the anvil simply rises as a buoyant parcel in response to the heating. In the real atmosphere, however, compensating downward motion will occur in the region around the anvil, producing adiabatic warming and contributing to a finite δT. A scale analysis of the complete set of equations (including horizontal momentum and continuity equations), in which a horizontal scale of 50 km, a vertical scale of 1 km, and a time scale of 2 h are assumed, shows that the ratio of the heating term to the vertical motion term in the equation above is about 0.1. This implies that to first order we may ignore the heating and treat the anvil as a buoyant parcel in a fixed environment. In this case, the vertical motion of the anvil is $w = (RQ)/(N^2 H)$ or about 3.3×10^{-2} m s^{-1} for an anvil-averaged heating rate of 30°K day^{-1}. In the typical anvil lifetime of about 6 hours observed in Panama, the system will rise about 700 meters. This is probably an upper limit, since the heating rates drop as the anvil dissipates. Higher ice water content only increases the net heating and vertical motion slightly, although the impact on vertical heating gradients is substantial.

The dynamical significance of the 3.3×10^{-2} m s^{-1} vertical motion can be seen by comparison with a radiatively-driven clear sky upward vertical motion of about 8.9×10^{-4} m s^{-1} in the 15–18 km region of the tropical lower stratosphere (assuming solar heating of 0.3°K day^{-1} and IR heating of 0.5°K day^{-1}). Consequently, even if high altitude anvils occupied only 1% of the horizontal area in the tropics, they could account for one-third of the total upward mass transport in this limited altitude range. Unfortunately, verification of anvil rise during the 1980 Panama experiment is inconclusive due to the presence of multiple anvil layers from different convective cells and the reversible undulations produced by gravity waves (Pfister et al. 1986).

Discussions of the vertical motion of the anvil must, of course, be tempered by the realization that the individual ice crystals have a fall velocity relative to the surrounding air. Typical values of the relative fall velocity of crystals with a maximum dimension of 50 μm (i.e., the crystals measured in the Panama study) range from about 1 to 10 cm s^{-1} depending on the shape of the crystal (Pruppacher and Klett 1978; Heymsfield 1972; Starr and Cox 1985a). Thus, in an hour the crystals would fall on the order of 35 to 350 m relative to the air parcel in which they are imbedded. This would in large part counterbalance, or possibly exceed, the parcel lifting discussed above. The more recent measurements during STEP suggest somewhat smaller ice crystals at cloud top with typical equivalent area diameters of 20 μm (personal communication, R. G. Knollenberg 1987), which would have slower fall velocities. Danielsen (1982b) has invoked the process of crystal sedimentation as a means of separating ice crystals from an ascending parcel at anvil top and thereby dehydrating air injected into the stratosphere. This process may also segregate particles vertically by size with the larger particles preferentially settling toward cloud base. However, Ramaswamy and Detwiler (1986) suggest that the larger crystals are always at cloud top because the crystals at cloud base are falling out of the saturated layer where formation occurs into an unsaturated region where sublimation occurs. Regardless of the exact vertical distribution of the various crystal sizes, the distribution is likely to have an important effect on the optical properties of the cloud since the smaller crystals have a larger extinction efficiency at the important window wavelengths.

The turbulent mixing generated by the radiative heating gradients has significance beyond the simple maintenance of an adiabatic lapse rate in the anvil. Convective elements impinging on inversions at the top and bottom of the anvil (for an example of the anvil thermal structure, examine the aircraft profile in Fig. 3 and the inversions at 15.6 and 17.4 km) may entrain air into the anvil, resulting in increases in anvil volume and changes in anvil temperature and water content. It is useful to compare radiatively driven entrainment with that due to other processes, such as vertical shear at the anvil boundaries. If we assume an anvil with an adiabatic lapse rate and equal inversion strengths and wind shears at both top and bottom, we can obtain an estimate of the entrainment velocity, w_e, at either boundary by analogy with the unstable boundary layer formulations of Stull (1976) and Stage and Businger (1981):

$$w_e = \frac{kBD^2}{12\delta\theta} + \frac{2a_3(1-b_3)\delta u^3\theta_0}{gD\delta\theta}. \tag{6}$$

Here D is the depth of the anvil; B the vertical radiative

heating gradient; $\delta\theta$ and δu the potential temperature and wind speed jumps, respectively, at both the top and bottom of the anvil; θ_0 the mean potential temperature of the anvil; and g the acceleration of gravity. The k, a_3 and b_3 are constants representing the generation and dissipation of turbulent kinetic energy (TKE) and are determined experimentally.

The first term on the right-hand side of Eq. (6) represents entrainment due to buoyancy production by the radiative heating gradient B. It is identical to the "vertically symmetric" case evaluated by Lilly (1988). The second term represents entrainment due to shear generation of TKE associated with equal velocity jumps δu at the top and bottom boundaries of the anvil. Equation (6) is analogous to Eq. (7) of Stull (1976), except for: (i) the parabolic (instead of linear) vertical heat profile (Lilly, 1988); (ii) the omission of the gravity wave losses (which Stull has shown to be small for strong inversions such as those in Fig. 3); and (iii) the assumption that conversion of TKE to potential energy by downward heat fluxes occurs throughout the turbulent anvil (as postulated by Stage and Businger 1981) rather than only in a thin layer near the upper boundary. The effect of this last assumption is to reduce the shear generation by the ratio of the depth of this thin layer to the total depth of the anvil [i.e., the D in the denominator of the second term on the right of Eq. (6)].

The radiative contribution to w_e can be estimated using parameter values consistent with the 1980 Panama observations and the computed heating rates (Figs. 3 and 4). Setting $B = 3.1 \times 10^{-7}$ K s^{-1}, $\delta\theta = 12$ K, $H = 2000$ m, and $k = 0.2$ (Stage and Businger 1981), we arrive at an entrainment velocity due to radiation of 0.0019 m s^{-1}. To estimate the shear contributions, we use $a_3(1 - b_3) = 0.0027$ (the midpoint of a large range of values given in Stull 1976), and $\delta u = 5.7$ m s^{-1} (the wind shift over a 100 m vertical layer at the inversion shown in Fig. 3; wind measurements were obtained from the radiosonde). This yields an entrainment velocity due to shear generation of 0.0018 m s^{-1}, which is comparable to the radiative component. Considering that entrainment occurs at both the top and the bottom of the anvil, the anvil depth will increase by roughly 50 m in about 2 hours, a negligible amount compared to the assumed thickness of 2 km. However, both the radiatively-driven and shear-driven w_e are subject to large uncertainties. For an IWC of 0.1 g m^{-3} (Fig. 6), rather than 0.02 g m^{-3}, the buoyant production would increase by a factor of 4. Also, a δu of 10 m s^{-1} would not be unreasonable for strongly sheared environments in the lower stratosphere. If both the higher IWC and shear were used in the calculations, the increase in anvil thickness in 2 hours could be as much as 300 m, or 15% of the initial anvil thickness.

The changes in average anvil temperature associated with the entrainment are probably small, since relatively cold air entrained at the bottom will be largely balanced by relatively warm air entrained at the top (for the case of the idealized thermal structure assumed above). This, however, is subject to the assumption of vertical symmetry in the downward heat fluxes at the top and bottom boundaries (Lilly 1988). Such symmetry may not be justified in the presence of strong shear generation, which is probably stronger at the anvil top than at the bottom. The effect of entrainment on the anvil's water content may be more important than the effect on the temperature since the air entrained at both top and bottom could be relatively dry. This might, in turn, affect the viability of the dehydration engine (Danielsen 1982b).

In conclusion, although it is interesting and useful to explore the dynamical implications of the heating rate profiles, it should be remembered that these are instantaneous heating rates. The temporal evolution of an anvil layer actually depends on a complicated interaction of infrared and solar radiative heating rates, ice microphysics, and dynamical motions on several scales (for example, see Starr and Cox 1985a,b). Both experimental data and time-dependent modeling are needed to sort out the importance of the various interactions in the anvil life cycle.

8. Effects on the energy budget

Cirrus clouds are an important component of the planetary energy budget because of their large spatial extent and their strong interaction with both the solar and infrared radiation fields. As noted above, cirrus clouds reduce the loss of infrared radiation from the planetary system. At the same time, they increase the amount of solar radiation lost from the system by enhancing solar backscatter. For small to moderate optical depths, the infrared effect, which is due to absorption by the ice crystals, dominates. At large optical depths, the solar effect, which is due to scattering, dominates. The exact cross-over point between energy gain and loss is a complicated function of particle shape, size, and number (which control cloud optical depth); cloud location and temperature; and solar zenith angle.

The effect of cirrus on the planetary radiation budget is illustrated in Fig. 13a where the reflected solar and emitted infrared radiation are plotted as a function of cirrus cloud optical depth at a reference wavelength of 0.55 μm. The cloud was fixed in altitude between 15 and 17 km and the optical depth was increased by increasing the assumed IWC. The solar calculations were carried out for a solar zenith angle of 53°, which is an appropriate daytime average for tropical latitudes, and a surface albedo of 0.05 which is consistent with tropical ocean values. The infrared flux begins to decrease noticeably for optical depths of a few tenths and approaches a limiting value (roughly corresponding to a brightness temperature of 194 K) at an optical depth of about 4. At this point essentially all the upwelling

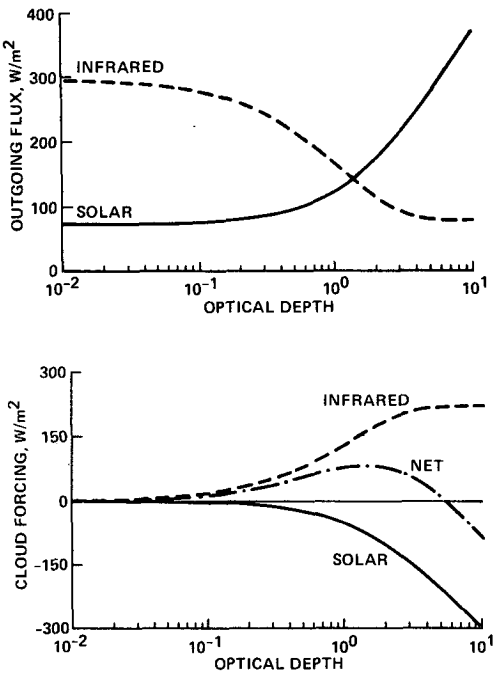

FIG. 13. (a) Emitted infrared and reflected solar flux and (b) infrared, net, and solar cloud forcing in W m^{-2} as a function of cirrus 0.55 μm optical depth. The cloud is assumed to be plane-parallel and located between 15 and 17 km altitude. The solar zenith angle is 53°.

radiation from the troposphere is absorbed and increasing the optical depth has no further effect. The reflected solar radiation begins to increase noticeably at an optical depth of about 0.5. At an optical depth of 10, the reflected solar radiation has increased by about a factor of 5 (for this particular value of the zenith angle).

The concept of cloud radiative forcing has been discussed in a number of recent papers (e.g., Ramanathan 1987; Slingo and Slingo 1987). For the solar spectrum, cloud forcing is simply the difference between the reflected solar radiation for clear sky and that for cloudy sky. Similarly, for the infrared spectrum, cloud forcing is the difference between the outgoing longwave radiation for the clear sky and for cloudy sky. In Fig. 13b the cloud forcing for solar and infrared radiation is plotted as a function of optical depth. The net cloud forcing, which is the sum of the two terms, is also plotted. As expected, the solar cloud forcing is always negative since the cirrus cloud increases the reflected solar radiation, while the infrared cloud forcing is always positive due to the reduction in infrared radiation loss. The net forcing, however, changes sign from positive to negative at an optical depth of about 5.

The change of sign in the net cloud forcing illustrates one of the important features of tropical cirrus. For most clouds, including midlatitude cirrus, cloud forcing is negative, i.e., the clouds reduce the amount of radiation absorbed by the planetary system. Cloud forcing due to tropical cirrus may be either positive or negative, depending on the optical depth. For small to moderate optical depths, the forcing is positive. At large optical depths, it becomes negative. Thus, in order to understand even the qualitative effect of cirrus clouds on the planetary radiation budget, we need to know their optical depth. As Slingo and Slingo (1987) point out, solar cloud forcing is felt mainly at the surface because the atmosphere is largely transparent to solar radiation. Since the tropical surface is mainly ocean, the effect of cirrus clouds is to reduce the direct heating of the ocean mixed layer. The infrared cirrus cloud forcing in the tropics, on the other hand, is largely confined to the atmosphere, particularly at the level of the cirrus itself. As we have shown, this forcing results in direct heating of the cloud layer itself.

It should be noted that the calculations shown in Fig. 13 are illustrative only since they were carried out for a particular set of assumed cloud properties and for plane-parallel clouds. A different set of cloud properties could change the relative ratio of infrared to solar optical depth, thereby changing the ratio of cloud forcing as a function of optical depth. Although cloud features in the tropics are large, their actual finite extent probably reduces the fraction of reflected solar radiation when compared to plane-parallel clouds. Finite cloud effects are likely to be less important in the infrared where absorption, rather than scattering, dominates. Also, extrapolating these results to large areas of the tropics is difficult because the appropriate value of cloud fraction or average optical depth is not known. The actual impact of cirrus clouds on the energy budget of the tropics can be assessed using satellite measurements of the earth radiation budget (e.g., Ramanathan 1987) or high-altitude aircraft measurements. We have obtained aircraft radiometer data as part of the Stratosphere Troposphere Exchange Project (STEP) and intend to utilize the data to study this problem further.

9. Conclusions

In this paper, we have addressed the interaction of tropical cirrus anvils with infrared and solar radiation, focusing mostly on infrared effects. Our results indicate that several parameters have important roles in determining both the total infrared heating and the heating rate profile within an anvil. Not unexpectedly, since it determines the cloud optical depth, the single most important parameter is the average ice water content. However, the vertical distribution of IWC, the depth of the anvil, and the cloudiness of the underlying atmosphere are also significant factors. Unfortunately, our knowledge of the actual values of these parameters is very limited. While an IWC of 0.02 g m^{-3} is deduced from a limited set of aircraft observations, IWCs higher by a factor of 5–10 can be inferred from satellite measurements. While information on the vertical distri-

bution of IWC within anvils can be obtained with lidar (Platt et al. 1984, 1987), the very limited amount of such data presently available makes it difficult to generalize. Also, both the geometric thickness of the anvil and the cloudiness of the underlying atmosphere are highly variable and dependent on the particular conditions associated with individual anvils.

Our calculations show that, on average, infrared radiation exchange heats tropical anvils. This is primarily the result of warm surface temperatures and cold tropopause temperatures in the tropics. For small to moderate IWC values, infrared heating occurs at all levels within the anvil. Larger values of IWC lead to strong cloud-top coolings and cloud-base warmings. The distribution of heating within the anvil is also strongly influenced by the assumed vertical distribution of IWC. Deep anvils do not show the strong cloud-base heating because both the cloud-base temperature and the air density are greater. Absorption of solar radiation at anvil top can also produce significant heating due to the large solar flux available at high tropical altitudes. Solar heating becomes increasingly important relative to infrared heating as the optical thickness of the anvil increases. Since the solar heating occurs at cloud top, it acts to reduce the convective instability induced by the infrared exchange and may impact the diurnal cycle of convection in the tropics.

Given the large heating-rate gradients, it is apparent that radiative destabilization will occur in anvils with limited vertical extent and moderate IWC. In deep anvils, the degree of radiatively induced convective mixing would not appear to be significant. The heating rate gradients may also induce dynamical responses which would tend to lift and spread the anvils. However, the lifting would be partially or entirely compensated by crystal settling, which in turn would impact both the vertical distribution of optical depth and particle growth.

Perhaps the most important conclusion which can be drawn from this study is the need for sophisticated models in order to properly simulate the anvil life cycle. Clearly, radiational heating is an important process. But this radiational heating can affect the anvil temperature profile, anvil dynamics on a variety of scales, and ice particle microphysics. These processes then in turn feed back into the radiational heating. The very complex interactions between radiational heating and ice microphysics are both particularly important and particularly difficult to model. Some beginnings on the modeling of this interaction have been made (Stephens 1983; Ramaswamy and Detwiler 1986) but more effort needs to be devoted to this subject.

Finally, our results also impact observational studies of tropical cirrus. Previous experiments have provided useful observations but, unfortunately, the observational set has been incomplete. Future programs should focus on obtaining a more comprehensive set of measurements including cloud ice water content, cloud extent, environmental conditions, and the radiation field itself.

Acknowledgments. We are indebted to a number of our colleagues for discussions on various aspects of this work. In particular, we would like to thank Drs. E. Danielsen, A. Heymsfield, D. Lilly, P. Russell, B. Toon, and R. Young for their comments on our results and on an earlier version of this manuscript. Dr. G. Stephens and another reviewer provided excellent reviews of our manuscript which improved the clarity and focus of the presentation. This study also benefited from the summer visit of one of us (TPA) to the Cloud Systems Division of NCAR.

REFERENCES

Ackerman, T. P., and F. P. J. Valero, 1984: The vertical structure of Arctic haze as determined from airborne net flux measurements. *Geophys. Res. Lett.*, **11**, 469–472.

Betts, A. K., 1973: A composite mesoscale cumulonimbus budget. *J. Atmos. Sci.*, **30**, 597–610.

Danielsen, E. F., 1982a: Statistics of cold cumulonimbus anvils based on enhanced infrared photographs. *Geophys. Res. Lett.*, **9**, 601–604.

——, 1982b: A dehydration mechanism for the stratosphere. *Geophys. Res. Lett.*, **9**, 605–608.

Doherty, G. M., R. E. Newell and E. F. Danielsen, 1984: Radiative heating rates near the stratospheric fountain. *J. Geophys. Res.*, **89**, 1380–1384.

ERBE Science Team, 1986: First data from the Earth Radiation Budget Experiment (ERBE). *Bull. Amer. Meteor. Soc.*, **67**, 818–824.

Griffith, K. T., S. K. Cox and R. G. Knollenberg, 1980: Infrared radiative properties of tropical cirrus clouds inferred from aircraft measurements. *J. Atmos. Sci.*, **37**, 1077–1087.

Houze, R. A., Jr., S. G. Geotis, F. D. Marks and A. K. West, 1981: Winter monsoon convection in the vicinity of North Borneo. Part I: Structure and time variation of the clouds and precipitation. *Mon. Wea. Rev.*, **108**, 1595–1614.

Johnson, R. H., and D. C. Kriete, 1982: Thermodynamic and circulation characteristics of winter monsoon tropical mesoscale convection. *Mon. Wea. Rev.*, **110**, 1898–1911.

Heymsfield, A., 1972: Ice crystal terminal velocities. *J. Atmos. Sci.*, **29**, 1348–1357.

Kley, D., A. L. Schmeltekopf, K. Kelly, R. H. Winkler, T. L. Thompson and M. McFarland, 1982: Transport of water through the tropical tropopause. *Geophys. Res. Lett.*, **9**, 617–620.

——, ——, ——, ——, —— and ——, 1983: The U-2 Lyman-α hygrometer results from the 1980 Panama experiment. The 1980 Stratospheric Tropospheric Exchange Experiment, A. P. Margozzi, Ed., NASA Tech. Memo. 84297.

Knollenberg, R. G., A. J. Dascher and D. Huffman, 1982: Measurements of the aerosol and ice crystal populations in tropical stratospheric cumulonimbus anvils. *Geophys. Res. Lett.*, **9**, 613–616.

——, —— and ——, 1983: Measurements of stratospheric aerosols and tropospheric/stratospheric ice-crystal populations during the 1980 Panama experiment. The 1980 Stratospheric Tropospheric Exchange Experiment, A. P. Margozzi, Ed., NASA Tech. Memo. 84297.

Lilly, D. K., 1988: Cirrus outflow dynamics. *J. Atmos. Sci.*, **45**, 1594–1605.

Liou, K. N., 1974: On the radiative properties of cirrus in the window region and their influence on remote sensing of the atmosphere. *J. Atmos. Sci.*, **31**, 522–532.

——, 1986: Influence of cirrus clouds on weather and climate processes: A global perspective. *Mon. Wea. Rev.*, **114,** 1167–1199.

Margozzi, A., Ed., 1983: 1980 Stratospheric Tropospheric Exchange Experiment, NASA Tech. Memo. 84297.

Meador, W. E., and W. R. Weaver, 1980: Two-stream approximations to radiative transfer in planetary atmospheres: A unified description of existing methods and a new improvement. *J. Atmos. Sci.*, **37,** 630–643.

Minnis, P., and E. F. Harrison, 1984: Diurnal variability of regional cloud and clear-sky radiative parameters derived from GOES data. Part II: November 1978 cloud distributions. *J. Climate Appl. Meteor.*, **23,** 1012–1031.

Newell, R. E., and S. Gould-Stewart, 1981: A stratospheric fountain? *J. Atmos. Sci.*, **38,** 2789–2796.

Paltridge, G. W., and C. M. R. Platt, 1976: *Radiative Processes in Meteorology and Climatology.* Elsevier, 318 pp.

Pfister, L., W. Starr, R. Craig, M. Loewenstein and M. Legg, 1986: Small scale motions observed by aircraft in the tropical lower stratosphere: Evidence for mixing and its relationship to large scale flows. *J. Atmos. Sci.*, **43,** 3210–3225.

Platt, C. M. R., A. C. Dilley, J. C. Scott, I. J. Barton and G. L. Stephens, 1984: Remote sounding of high clouds. V: Infrared properties and structures of tropical thunderstorm anvils. *J. Climate Appl. Meteor.*, **23,** 1296–1308.

——, J. C. Scott and A. C. Dilley, 1987: Remote sounding of high clouds. VI: Optical properties of midlatitude and tropical cirrus. *J. Atmos. Sci.*, **44,** 729–747.

Pollack, J. B., and T. P. Ackerman, 1983: Possible effects of the El Chichon cloud on the radiation budget of the northern tropics. *Geophys. Res. Lett.*, **10,** 1057–1060.

——, and C. P. McKay, 1985: The impact of polar stratospheric clouds on the heating rates of the winter polar stratosphere. *J. Atmos. Sci.*, **42,** 245–262.

Pruppacher, H. R., and J. D. Klett, 1978: *Microphysics of Clouds and Precipitation.* Reidel, 714 pp.

Ramanathan, V., 1987: The role of earth radiation budget studies in climate and general circulation research. *J. Geophys. Res.*, **92,** 4075–4096.

Ramaswamy, V., and A. Detwiler, 1986: Interdependence of radiation and microphysics in cirrus clouds. *J. Atmos. Sci.*, **43,** 2289–2301.

Slingo, A., and J. M. Slingo, 1987: The response of a general circulation model to cloud longwave radiative forcing. I: Introduction and initial experiments. *Quart. J. Roy. Meteor. Soc.*, submitted.

Stage, S. A., and J. A. Businger, 1981: A model for entrainment into a cloud-topped marine boundary layer. Part I: Model description and application to a cold-air outbreak episode. *J. Atmos. Sci.*, **38,** 2213–2229.

Starr, D. O'C., and S. K. Cox, 1985a: Cirrus clouds. Part I: A cirrus cloud model. *J. Atmos. Sci.*, **42,** 2663–2681.

——, and ——, 1985b: Cirrus clouds. Part II: Numerical experiments on the formation and maintenance of cirrus. *J. Atmos. Sci.*, **42,** 2682–2694.

Stephens, G. L., 1980: Radiative properties of cirrus clouds in the infrared region. *J. Atmos. Sci.*, **37,** 435–446.

——, 1983: The influence of radiative transfer on the mass and heat budgets of ice crystals falling in the atmosphere. *J. Atmos. Sci.*, **40,** 1729–1739.

Stull, R. B., 1976: Mixed-layer depth model based on turbulent energetics. *J. Atmos. Sci.*, **33,** 1268–1278.

Toon, O. B., J. B. Pollack and C. Sagan, 1977: Physical properties of the particles composing the Martian dust storm of 1971–1972. *Icarus,* **30,** 663–696.

——, C. P. McKay, T. P. Ackerman and K. Santhanam, 1988: Rapid calculation of radiative heating rates and photodissociation rates in inhomogeneous multiple scattering atmospheres. *J. Geophys. Res.*, submitted.

Warren, S. G., 1984: Optical constants of ice from the ultraviolet to the microwave. *Appl. Optics,* **23,** 1206–1225.

Webster, P. J., and G. L. Stephens, 1980: Tropical upper troposphere extended clouds: Inferences from Winter MONEX. *J. Atmos. Sci.*, **37,** 1521–1541.